Laser-driven ion acceleration in presence of increasing heating of relativistic electrons at steep overdense plasma interfaces

Stefan Hüller, Anna Porzio, Anne Héron, Patrick Mora

Laser-driven ion acceleration in presence of increasing heating of relativistic electrons at steep overdense plasma interfaces

S. Hüller,[1] A. Porzio,[2,1] A. Héron,[1] and P. Mora[1]
[1)] *Centre de Physique Théorique(CPHT), CNRS, Ecole Polytechnique, IP Paris, 91128 Palaiseau, France*
[2)] *LAGA, Institut Galilée, Université Paris 13, Villetaneuse, France*

The role of the density gradient in the electron acceleration process by intense laser pulses for a plasma profile with a steep interface between vacuum and a strongly overdense plasma is investigated via particle-in-cell simulations with the EMI2D code. Laser pulses at relativistic intensities interacting with finite gradients at the laser-plasma interface favour collective electron motion in the underdense plasma provided that the pulse duration is long enough to form a standing wave structure. It is shown that the steepness of the gradient has an influence on the evolution of the distribution of electrons that are injected into the dense plasma. Heating mechanisms of the electron bulk and of a very energetic electron tail are identified. The heating of the targets evolves each time when bunches of electrons accelerated to relativistic energies return to the laser-plasma interface. The heating dynamics has consequences on the ion front motion at the rear of the target. This is elaborated by determining the predominant hot electron populations and their temperatures which govern the expansion of the rear density profile. The role of the temporal dynamics of the hot electron populations is investigated with respect to the known analytic models for ion acceleration at the rear target, showing that those models are robust despite important temporal increase of hot electron temperatures.

I. INTRODUCTION

Ultra-intense laser pulses that impinge on a dense plasma target can accelerate electrons to highly relativistic energies such that they can penetrate into a dense target. When those electrons arrive at the rear face of the dense target, rarefaction of the plasma profile[1,2] and strong charge separation effects[2,3] lead to the acceleration of the plasma ions. The ion acceleration process depends on the efficiency of the conversion of the laser energy into electron heating, and, according to models[2–9] on the temperature of the hot electron tail of the distribution. Imprint of micro structure and/or of the excitation of surface modes on the dense target surface has been investigated to improve the conversion efficiency in order to inject electrons into the dense plasma.[10–15] In recent work by Héron et al.[16] it was found that a density gradient at the interface where the intense laser pulses impinges on the dense target may act favourably for conversion in kinetic energy. While today electron acceleration is considered in the relativistic laser intensity regime, the latter process is well known already from the non-relativistic regime, even related to wave conversion processes, both in their linear and non linear stage[17–19].

Heating of electrons is known from the 1970's via resonance absorption, mostly for the case of obliquely incident and p-polarized laser light for the case of non-relativistic intensities[17,18]. At higher intensity, and in particular when profile steepening arises, other processes come into play[19]. For the case of relativistic laser intensities, with a pre-plasma in front of the critical density, the electron acceleration has been revisited by Kemp et al[20], taking into account ponderomotive heating[21] and profile steepening, and recently in conjunction with experiments[22–25]. The regimes of relativistic and sub-relativistic standing-wave acceleration of electrons due to laser light reflection have been investigated and identified in experiments and via simulations in Ref. 26.

In this article we focus on the production of hot electron populations and the acceleration of ultra-relativistic electrons around a steep laser-plasma interface. We pay particularly attention on the role of the plasma profile with respect to the ion acceleration at the rear of the target due to the modification of the electron distribution by those laser-induced electron heating mechanisms. The laser pulses considered have a duration such that a standing wave structure forms in front of the target due to partially reflected light.

The results presented are based on particle-in-cell (PIC) simulations with the code EMI2D[27] developed by J. C. Adam and A. Héron at CPHT, in a version with 2 dimensions in the configuration- and 3 in momentum space (2D3V). The simulation configurations are based on target of thickness between $150k_0^{-1}$ and $300k_0^{-1}$ and width of $27k_0^{-1}$, with $k_0 = \omega_0/c$ standing for the vacuum wave number for the laser with the frequency ω_0. Simulation run times last up to $2000\omega_0^{-1}$, corresponding to 800-1000fs for frequencies ω_0 of lasers wave lengths in the range 0.8-1μm, such that relativistic electrons emitted at the interface can, a priori, return repeatedly from the rear face of the target.

The interactions in such configurations are complex, with respect to both the effects along the target surface and the effects inside the dense target with return current effects and magnetic field generation[28]. We concentrate here on the electron and ion motion, as well as on the fields in the direction of laser propagation, with normally incident laser light. In the majority, the results are presented in the spatial average over the dimension y perpendicular to the laser axis.

In a preceding publication[29] we have shown that the multi-dimensional nature of the acceleration processes is

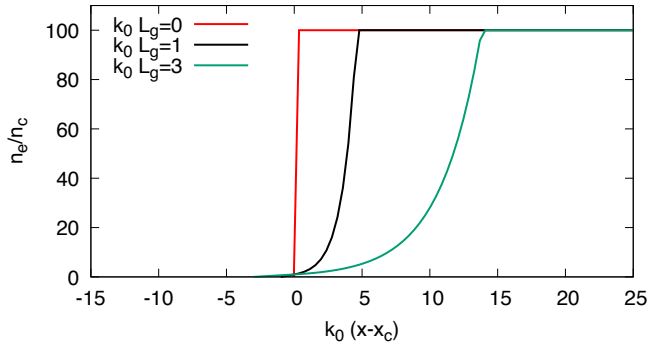

FIG. 1. Density profiles n_e/n_c as a function of x at the plasma interface for three different gradient lengths L_g at the critical density following the profile shape following Eq. (1).

crucial for the production of energetic electrons for intense laser pulses. In this article we have shown that energetic electrons ejected from the laser-dense plasma interface into the direction of the incoming laser are subject to successive stochastic acceleration[22,30–33]. Stochastic acceleration is explained by the non linear motion in the standing wave field[34,35] formed by the incident and reflected light. In first approximation, this acceleration process can be simplified to 1D geometry. However, the light fields do not have a plane wave structure due to upcoming filamentation which is eventually the reason why a certain population of energetic electrons can be ejected into the vacuum region, otherwise impossible in 1D geometry[23,36,37].

While in this preceding work we have initially considered an abrupt density jump, we investigate here aspects that appear when the plasma density gradient is finite. The latter can be characterized by the electron density gradient length $L_g = (n_e/\partial_x n_e)|_{n_e=n_c}$ at critical density n_c where the plasma frequency, ω_{pe} equals the laser frequency, i.e. $\omega_0 \equiv \omega_{pe}(n_e = n_c)$. Kemp et al. in Refs. 20 and 38 underline that the physics at the interface changes considerably in presence of a pre-plasma which appears intrinsically with a finite density gradient. Although ponderomotive profile steepening will dynamically limit the gradient L_g^{-1} at critical density, an underdense "foot" of electron population will result in collective oscillations of those electrons in the superposed (incident and reflected) light field. As explained in what follows, only a small portion of the electrons in such a pre-plasma are super-relativistic, such that the resulting heating process is different from stochastic acceleration.

The gradient scale length of the pre-plasma has been shown to be important for the angular divergence of the emerging energetic electrons[39] which involves also induced magnetic fields[40]. The influence of gradient length on the electron spectra in the context of ultrashort pulses (30fs) has also been studied in conjunction with experiments.[41]

Our article is organized as follows: in section II, after defining the configurations of the plasma profiles used,

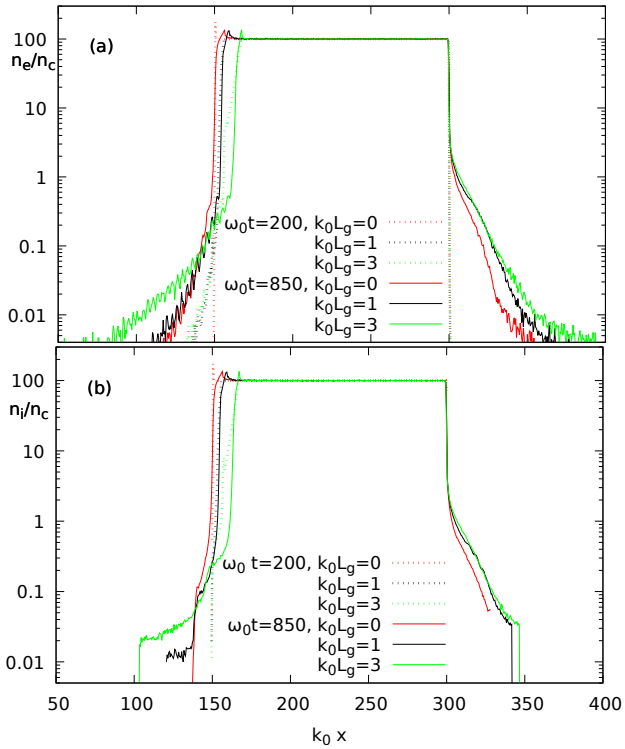

FIG. 2. (a) Electron and (b) ion density profiles $n_{e,i}/n_c$, averaged over y, as a function of x, for times $\omega_0 t$ =200 and 850 for three cases $k_0 L_g$ =0,1, and 3 (red, black, and green lines respectively) with x_c=150k_0^{-1} and thickness 150k_0^{-1}.

we illustrate via phase space snap shots from PIC simulations and the resulting distribution functions the essential features of acceleration processes in comparing plasma profiles with an abrupt jump up to $100n_c$ ($k_0 L_g$ =0) and profiles having a finite gradient $k_0 L_g$ =1 or 3. In section III we analyze the formation of hot electron populations and determine the corresponding temperatures. In section IV we demonstrate the robustness of the model for ion acceleration at the rear of the target, before concluding with discussions.

II. EMI2D SIMULATIONS

A. Simulation set up

We have performed simulations with the PIC code EMI2D[27] with a laser pulse with a ramp in time that reaches its maximum intensity after $\omega_0 t = 50$. The pulse then keeps this maximum value until the end of the simulation. The time instant t =0 corresponds to the moment when the laser pulse enters the simulation box at x =0. The simulation boxes have a width of 27k_0^{-1} and a length of 550k_0^{-1} or 800k_0^{-1} for the target thickness of 150k_0^{-1} or 300k_0^{-1}, respectively. For the relatively small box width, the incoming laser light is modeled by an incoming plane wave. The components of the electromagnetic field solver are E_x, E_y, and B_z, hence two-dimensional (2D, x,y) geometry, while the particle motion is 2D in configuration

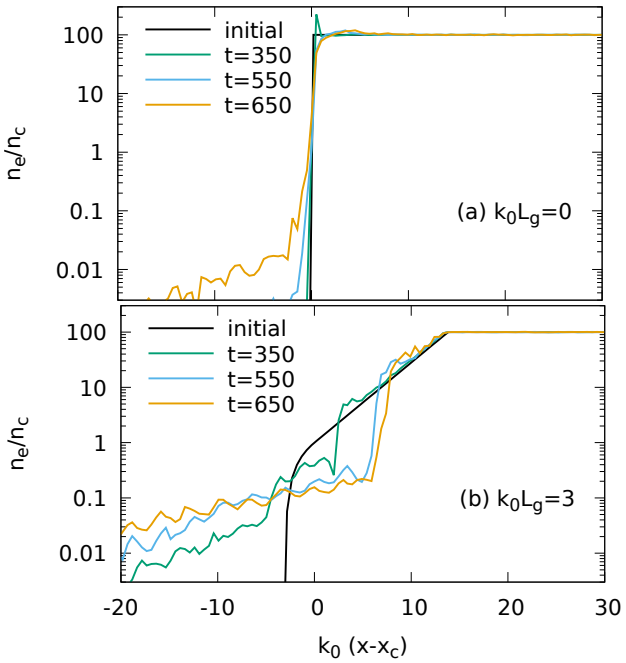

FIG. 3. Electron density profiles n_e/n_c, averaged over y, as a function of x, around the vacuum plasma interface at x_c=150, for three different times and for the cases (a) of an initially step-like profile (k_0L_g =0) and (b) of an initial exponential density profile density with $k_0L_g = 3$. A non-negligible pre-plasma at low density ($< 0.03n_c$) forms lately, with a stronger spatial extension and density ripples for case (b).

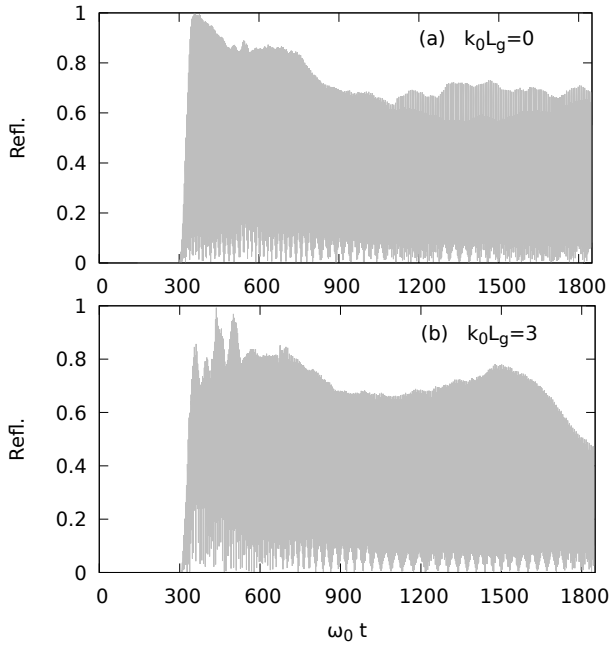

FIG. 4. Time evolution of the reflected light flux for the cases $k_0L_g = 0$ (top) and $= 3$(bottom). The onset time of $\omega_0 t \sim 300$ corresponds to twice the propagation time of the incoming laser pulse to reach the interface. .

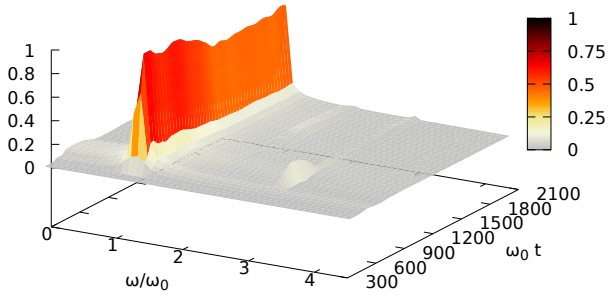

FIG. 5. Time evolution of the reflected light flux (in arbitrary units), spectrally analyzed for the case $k_0L_g = 0$ as a function of time and of the frequency in multiples of the laser frequency. The onset time of $\omega_0 t \sim 300$ corresponds to twice the propagation time of the incoming laser pulse to reach the interface. The amplitude unit of ~ 900 corresponds to 100% reflection in Fig. 4. .

space (x,y), but three-dimensional (3V) in momentum space, allowing for the components p_x, p_y, p_z for the electrons, $v_{i,x}$, $v_{i,y}$, $v_{i,z}$ for (here non-relativistic) ions. Periodic boundary conditions are assumed in the direction perpendicular to the incoming laser light whose electric field, with the peak amplitude E_L, is linearly polarized in y-direction. The intensity value applied corresponds to a normalized vector potential amplitudes a_0 $[= eE_L/(m_e c\omega_0)] = 2.8$. The plasma interface situated around $150k_0^{-1}$ reflects the plane wave of the incoming laser light such that for $\omega_0 t >$150 a standing wave structure between incident and reflected light fields starts to form. The thickness of the target was chosen such that only fast particles can transverse the bulk, but no fields, namely between $150k_0^{-1}$ and $300k_0^{-1}$. At maximum density, 200 particles per cell of the size $\Delta x = \Delta y = 0.015k_0^{-1}$ were used. Rarefaction on both sides remains uncoupled over the simulation duration. The simulations were performed with mobile ions, without applying collisions, in a hydrogen plasma with an initial electron thermal speed of $v_{th,e}$ =0.03c (T_e = 230eV) and an ion/electron temperature ratio of T_i/T_e =0.1. Outgoing electrons are reflected at the front and at the rear boundaries. Within the simulation time, no ions exit the simulation domain.

B. Pre-plasma formation: step profile vs. gradient

Figure 1 illustrates the initial front profiles chosen at the plasma interface, with a step-like shape, up to $n_{\max}$ (here $100n_c$) and, alternatively exponentially increasing profiles between $n_e = n_c$ and $n_{\max}$, for which a linear

ramp has been chosen for lower densities, as defined by

$$\frac{n_e(x)}{n_c} = \begin{cases} 0 & \text{for } x-x_c < -L_g, \\ 1+\frac{x-x_c}{L_g} & \text{for } -L_g < x-x_c < 0, \\ e^{(x-x_c)/L_g} & \text{for } 0 \le x-x_c < L_g \log \frac{n_{\max}}{n_c}, \\ 100 & \text{for } x-x_c \ge L_g \log \frac{n_{\max}}{n_c}\ , \end{cases} \tag{1}$$

with x_c denoting the position of the critical density n_c. The step-like profile corresponds hence to $L_g \to 0$.

The entire density profiles of electrons and ions (here charge $Z = 1$) are illustrated in Figs. 2, respectively, for three cases with initially different gradients, namely, $k_0 L_g = 0$ (red lines), $= 1$ (black), and $= 3$ (green), for two time instants, $\omega_0 t$ =200 (early, dashed lines) and =850 (solid lines). The values shown are averaged over the whole width of the second dimension y in the 2D simulation. While electron profiles are oscillatory in front of the interface, and noisy at the rear of the target, the ion profiles show a clear front of expansion on each side. Figure 3 illustrates how an initially step-like profile and how an exponential profile evolve with ongoing time. While the step-like profile keeps a very steep gradient around $x = x_c = 150 k_0^{-1}$ with $n_e(x_c) = n_c$, a low-density foot with $n_e < 0.1 n_c$ develops as pre-plasma for $x < x_c$. For the exponentially-shaped profile the low-density foot occurs quite earlier and at higher densities. On the other hand, the initial gradient, here $L_g^{-1} = k_0/3$ steepens considerably and the position of the critical density is shifted towards higher values in x due to the light pressure.

C. Acceleration and heating in the steep front layer

As a consequence of the different profiles in the "pre-plasma" , the electron distribution function evolves with different temporal dynamics, related to the degree of reflected light, Fig. 4. The laser light is initially completely reflected for the case of the steep interface with $k_0 L_g$ =0, leading to a standing wave pattern in the pre-plasma, with a gradual decrease in the reflectivity R (defined as $\equiv |B_z(x=0)/B_{z,in}|^2$) up to $\omega_0 t \simeq 350$. During a transient period from $300 < \omega_0 t < 600$ the spectral content of the reflected signal exhibits also higher harmonics, with the highest level of ∼10% for the third harmonic, as seen in Fig. 5. These harmonics are due to non linear electron motion, a reminiscence of the oscillating mirror associated with such steep boundaries[42]. The second harmonic only occurs for the case with an initial step-like interface, $k_0 L_g = 0$, for later times for $\omega_0 t > 1000$. Both subplots in Fig. 4 show after a transient period another drop in the reflectivity shortly after $\omega_0 t = 700$. With this decrease in reflectivity from $R > 85\%$ to $R \simeq 70\%$, the uneven harmonics drop considerably. Phase space snapshots of the electron momenta p_x versus x, are illustrated in Figs. 6 and 7 for the cases of a step-like profile and a profile with gradient, namely $L_g = 3 k_0^{-1}$, respectively, both taken at similar times. The color bars

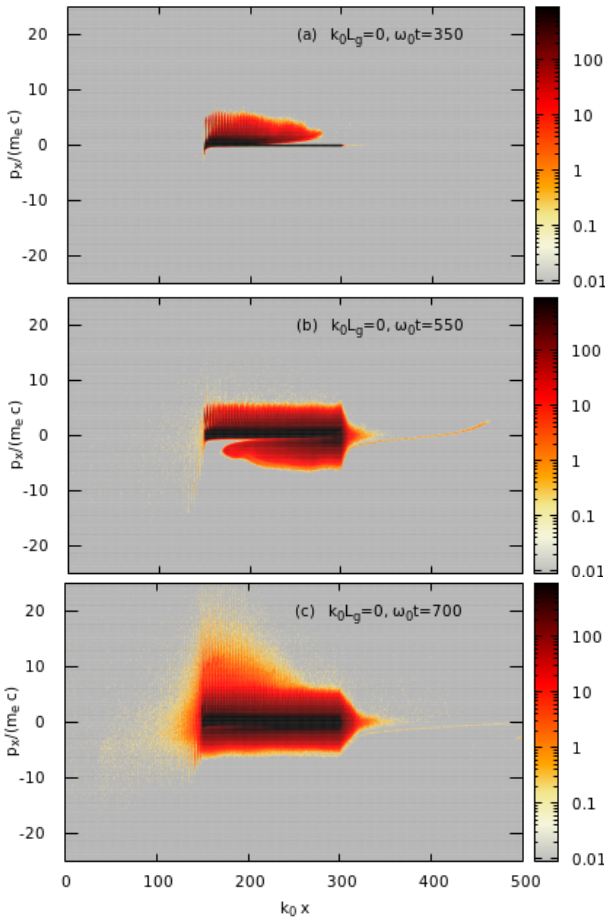

FIG. 6. Phase space contour snap shot in x-p_x, taken at $\omega_0 t$ =350 (a), 550 (b), and 700 (c) for the case of an initially step-like profile with $a_0 = 2.8$, x_c =150k_0^{-1}. The color map is highly saturated for contour values (not normalized) >300 in order to emphasize the population of high energy electrons.

for the phase space contours are chosen with the purpose to highlight the essential physics in the front of the high density plasma bulk. The contours in the bulk are therefore not resolved; their values are not normalized. For both cases one can observe an ondulation in the electron phase space contours, seen in the x-p_y phase space, Fig. 8, following the standing wave pattern formed by the superposition of the incident laser field and the reflected light. The number of particles, consistent with the observation concerning Figs. 3, is higher for the case with gradient. In the x-p_x phase spaces a clear signature of the stochastic acceleration mechanism[30,31,36] can be identified, as worked out in our previous work[29], for which the momenta $|p_x|$ of energetic electrons are gradually increased each time with a change in sign of p_x. For the cases with a finite density gradient, the acceleration process proves to arise earlier in time so that energetic, but moderately relativistic electrons arrive earlier at the rear of the target. Those electrons consequently are redrawn earlier in the opposite direction. Kemp et al.[20,38]

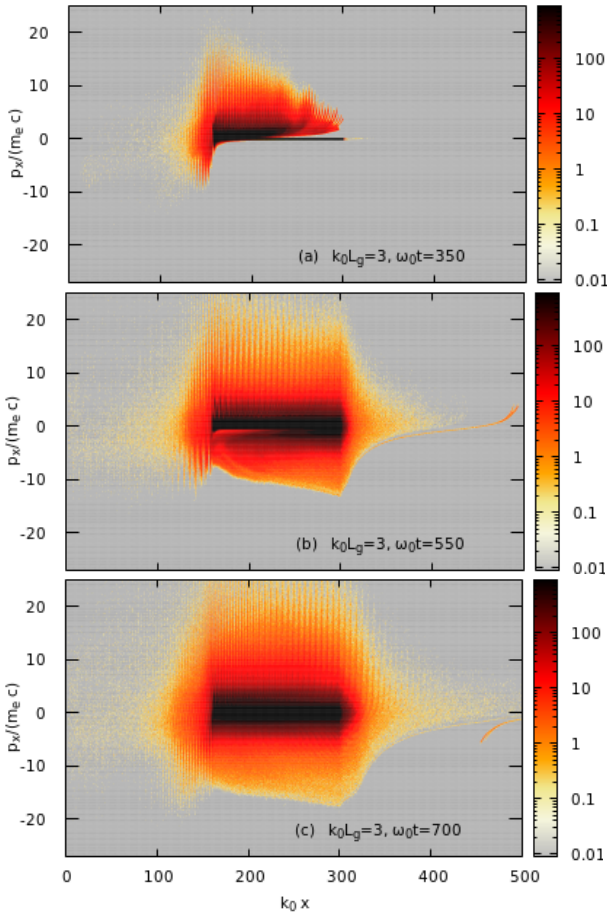

FIG. 7. Phase space contour snap shot in x-p_x, taken at $\omega_0 t$ =350 (a), 550 (b), and 700 (c) for the case of an initially exponential profile ($k_0 L_g$ = 3), both with a_0 = 2.8, x_c =150k_0^{-1}. The color map is highly saturated for >300 in order to emphasize the population of high energy electrons.

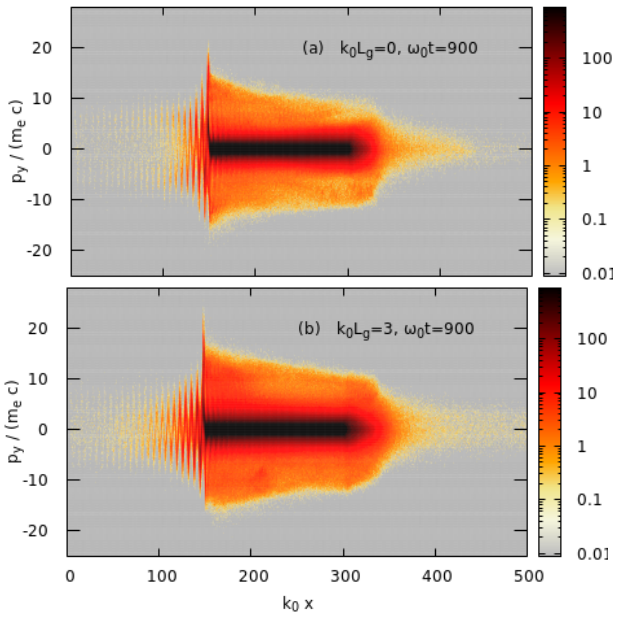

FIG. 8. Phase space contour snap shots in x-p_y for the cases (a, top) $k_0 L_g$ = 0 and (b, bottom) $k_0 L_g$ =3 taken at $\omega_0 t$ =900. The color map is highly saturated for >300 in order to emphasize the population of high energy electrons.

have studied in detail the heating process for such profiles by showing that bulk heating occurs in the layer of the gradient, associated with ponderomotive effects.

The bulk heating proves to be more efficient in presence of a gradient in front of the plasma interface, which is coherent with the lower reflectivity, and thus higher absorption efficiency, seen in Fig. 4(b). The bulk electrons can be identified by the width of the saturated (black color) bulk in the x-p_x phase space in Fig. 7, which is more pronounced for the case $k_0 L_g$ =3 with respect to $k_0 L_g$ =0, which is also seen when inspecting instead the x-p_y phase space dominated by the electron quiver motion in the polarization direction of the laser fields, see Fig. 8. The formation process of ultra-relativistic electrons, due to stochastic heating in the front part, is present also for the cases with developed gradients but it may initially be masked by the dominant heating of the electron bulk. The differences seen in Fig. 9 for the electron density, taken in the front part of the laser-plasma interface and at $\omega_0 t$ =700, between the cases $k_0 L_g$ =0 and 3, illustrate that at this stage the acceleration processes depend still on the initial gradient. The two-dimensional surface structures around the critical density, induced by filamentation, are correlated both with harmonic generation and the periodic heating which cannot arise in 1D geometry[29,36]. At the rear of the target (not shown here) no structure in y remains in the electron and ion density. Another mechanism that can come into play for gradients lengths $L_g > 0$, is the mechanism described Ref. 43 arising in the vicinity of the skin depth of thin layers.

D. Electron distributions

The acceleration mechanisms observed in the front layer, depending on the profile gradient, have consequences on the electron distribution functions. To illustrate this, we have determined the distribution densities for both $f(p_y)$ and $f(p_x)$ for the cases of an initially step-like profile and a profile with gradient. The early evolution of the electron heating is different in the momentum space components p_x and p_y, as shown for the electron distribution densities $f(p_x)$ and $f(p_y)$ in Fig. 10 obtained from the x-p_x and x-p_y phase spaces for a simulation with $k_0 L_g$ =0 and for a 300k_0^{-1} thick target, taken in the interval 200< $k_0 x$ <300 close to the laser-plasma interface at $k_0 x$ =150 (rear at $k_0 x$ =450). The heating in the p_x component in an first stage occurs in the positive direction until the first hot electrons that arrive at the rear are drawn back from the ambipolar field. For the x interval shown in Fig. 10(a) heated electrons with p_x <0 will therefore not arrive before times

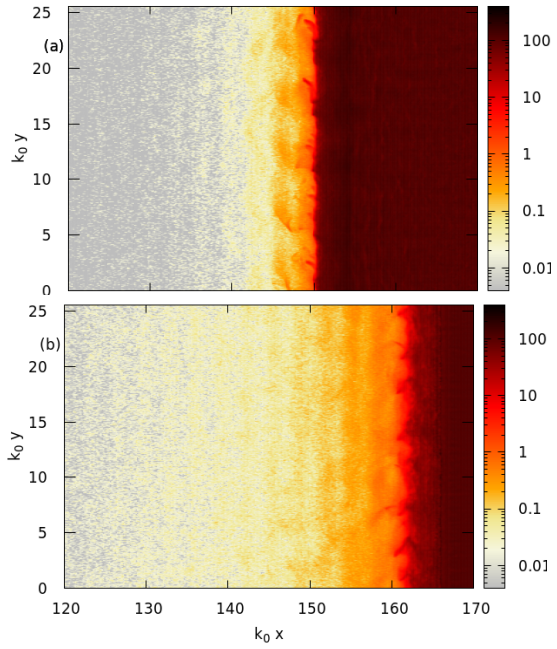

FIG. 9. Electron density n_e/n_c in x and y, in the vicinity of the laser-plasma interface, for the cases (a, top) $k_0L_g = 0$ and (b, bottom) k_0L_g =3 taken at $\omega_0 t$ =700.

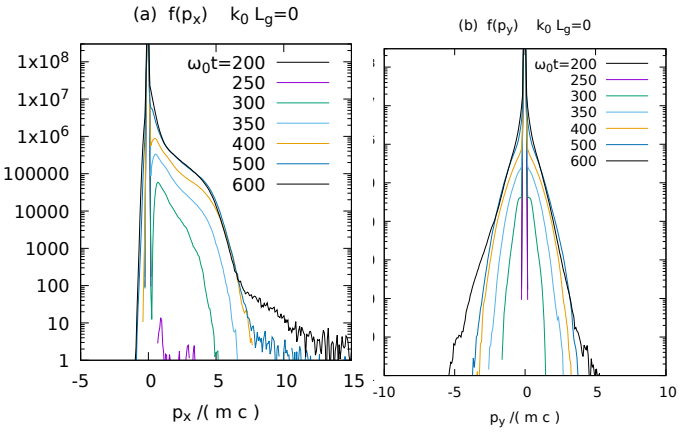

FIG. 10. Electron distribution density $f(p_x)$ (a, left) and $f(p_y)$ (b, right) as a function of the electron momenta p_x and p_y, respectively, at different time instants in the early stage of the interaction taken in the bulk of the plasma (200< k_0x <300); for a target of thickness $300k_0^{-1}$ and for the case with a density profile with a jump between $n_e = 0$ and $n_e = 100n_c$ at $x = x_c$ (i.e. $k_0L_g = 0$)

$\omega_0 t$ =600 (=150+300+150, with 150 for the time the laser pulse needs to reach the target interface, 300 for the target thickness, and 150 for the return path to the position where $f(p_x)$ is taken). The heating in p_y is from the beginning almost symmetric due to the regular oscillatory character in the laser field. As illustrates Fig. 11, taken in the spatial interval behind the interface, 180< k_0x <280, the bulk of the electron distribution widens slowly in p_y for k_0L_g =0 up to times $\omega_0 t$ ∼500, after which, as shows Fig. 12, ultra-relativistic energy tails emerge, in particular for positive p_x/m_ec values > 10, and later beyond p_x/m_ec = 20. This corresponds to what has been observed for stochastic acceleration[29], for which a standing wave pattern due to superposition of the incoming and reflected laser light fields is essential.

For the case of an initially exponential profile, k_0L_g =3 in Fig. 11(b), the widening of the bulk of the electron distribution occurs faster, which apparently goes hand in hand with a faster onset of the ultra-relativistic energy tail in $f(p_x)$, see Fig. 12. Apparently, for similar times, the distributions of the case with an exponential profile produce systematically higher $f(p_x)$-values in the range $|p_x|$ <10, resulting in a more efficient heating of the electron bulk. Due to the fact that not too short laser pulses continue to heat the plasma from the front side, the particle distribution evolves with a tendency to reinforce the population of energetic electrons. In a general manner, the distributions in Figs. 11 and 12 show that the dynamics of the electron heating mechanisms for the initially step-like profile, k_0L_g = 0, is delayed with respect to profiles with an already developed gradient. The heating is also linked to multi-dimensional effects.

The distributions as a function of p_x show the effect of a return current of the order of $\sim -0.02c$ in the bulk. This return current is linked to the generation of magnetic field components seen predominantly in the vicinity of the laser-plasma interface.[28,40]

III. FORMATION OF HOT ELECTRON POPULATIONS

The arrival of heated electrons at the rear of the target is important for the eventual expansion of the profile there, starting from the moment when heated electron populations dominate the dynamics. The goal of this

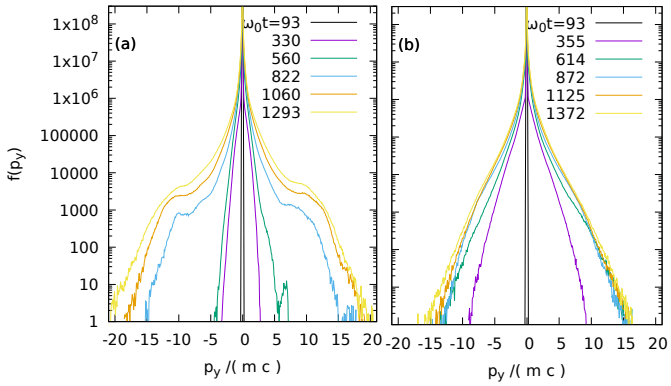

FIG. 11. Electron distribution density $f(p_y)$, at different time instants taken in the bulk of the plasma (180< k_0x <280), as a function of the electron momentum $p_y/(m_ec)$. (a), left : for a profile with a step-like density profile (k_0L_g =0); (b), right :for a density profile with a gradient between $n_e = 0$ and $n_e = 100n_c$ around $x = x_c$ (i.e. $k_0L_g = 3$).

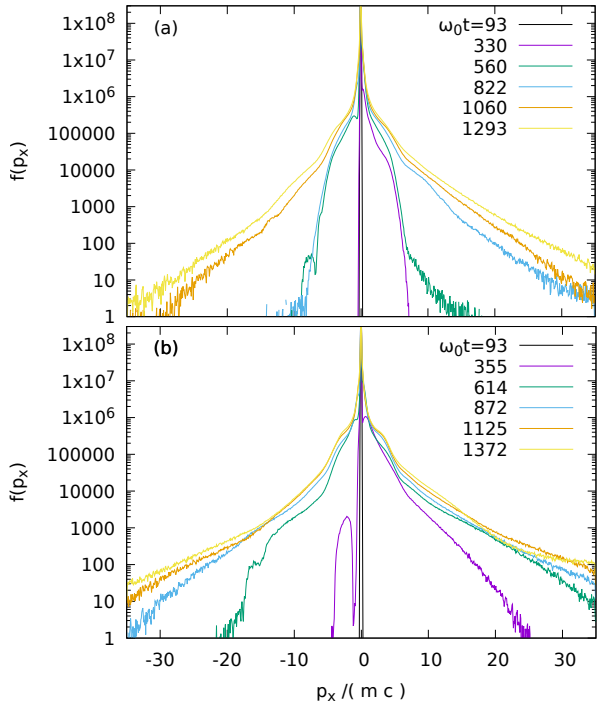

FIG. 12. Electron distribution density $f(p_x)$, at different time instants taken in the plasma behind the interface ($180< k_0x <280$), as a function of the electron momentum $p_x/(m_ec)$. (a), top for k_0L_g =0; (b) bottom for $k_0L_g = 3$.

section is to characterize the hot electron dynamics in order to eventually link it to the plasma expansion at the rear of the profile.

The distributions shown in the preceding sub-section have substantial presence of relativistic electrons. For distributions associated with a unique hot electron temperature one can use the relativistic extension of the Gauss/Maxwell distribution, namely the Maxwell-Jüttner[44] (MJ) distribution for which the probability density function (*pdf*) is given characterized by

$$f_{MJ}(\gamma) \propto e^{-\epsilon(\gamma)/k_BT_h} p(\gamma)^{d-1} dp/d\gamma \qquad (2)$$

with $p(\gamma) = \sqrt{\gamma^2 - 1}$, $\epsilon(\gamma)/k_BT_h \equiv \gamma/\theta_h = \gamma m_e c^2/k_BT_h$, considering motion in d dimensions and $dp/d\gamma = (1 - 1/\gamma^2)^{-1/2}$. For such type of distributions, the resulting expectation values γ_{MJ} and p_{MJ} can be related to the hot electron temperature, namely, for the entire interval $0\leq p <\infty$ ($1 \leq \gamma <\infty$).

For the current case of an almost one-dimensional expansion dynamics at the rear of the target, we consider the motion of hot electrons essentially in positive x-direction so that d =1. The integral for the expectation value γ_{MJ} as a function of $\gamma \geq 1$, namely $\gamma_{MJ} \equiv \int_1^\infty \gamma\, f_{MJ}(\gamma) d\gamma \equiv \int_1^\infty e^{-\gamma/\theta_h} \gamma (dp/d\gamma) d\gamma / K_1(\theta_h^{-1})$ yields then a relation to θ_h via

$$\gamma_{MJ} = \theta_h + K_0(\theta_h^{-1})/K_1(\theta_h^{-1}) \ , \qquad (3)$$

with K_n denoting the modified Bessel function of the 2nd kind. In the sub-relativistic case, namely $\gamma_{MJ} < 1.4$, the latter expression can be approximated by $\gamma_{MJ} \simeq \theta_h + (1 - \theta_h/8)/(1 + 3\theta_h/8)$.

In the ultra-relativistic case, $\gamma_{MJ}^2 \gg 1$, we can use the fact that Eq. (2) together with $dp/d\gamma \to 1$ results in a purely exponential law for which the integral yields a simple relation between the value of γ_{MJ} and the hot electron temperature, namely $\theta_h \simeq \gamma_{MJ} - 1$.

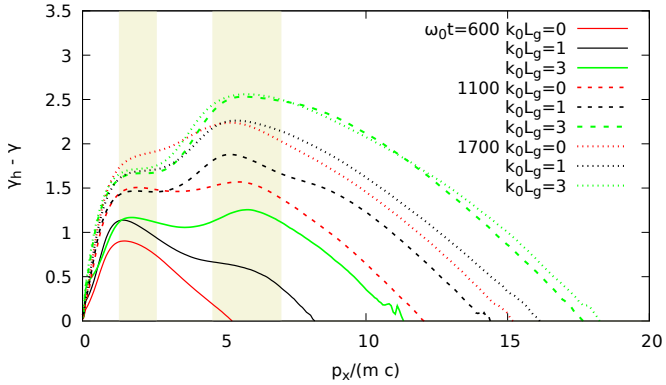

FIG. 13. Difference $\gamma_h(\gamma) - \gamma$ between the expectation value $\gamma_h(\gamma)$, defined in Eq. (4), and γ, for distinct times $\omega_0 t$ =600 (solid lines), 1100 (dashed), and 1700 (dotted). Plateau-like behavior as a function of p_x develops in the p_x-intervals of $1.5 < p_x/(m_ec) < 2.5$ and $5< p_x/(m_ec) <7$, as indicated by the shaded areas. The values are deduced from the distribution functions $f(p_x)$ corresponding to the $x - p_x$ phase space over the spatial interval $190< k_0x <290$ at the rear of the target, for k_0L_g =0(red lines), 1(black), and 3 (green).

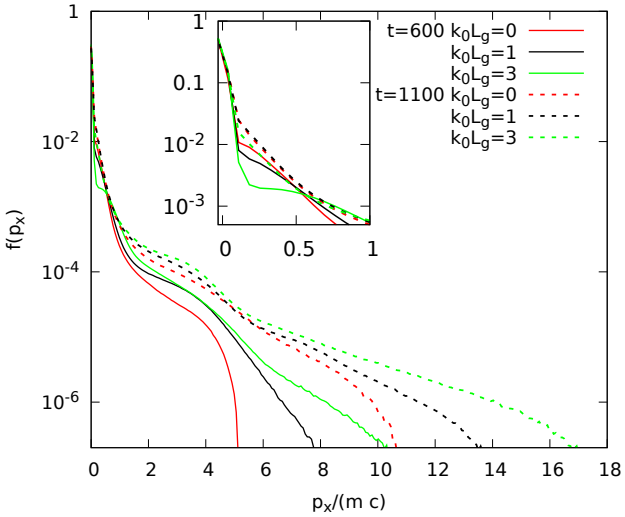

FIG. 14. Distribution density $f(p_x)$ for $p_x \geq 0$ in the interval for times $\omega_0 t$ =600 (solid lines) and 1100 (dashed), deduced from the distribution functions corresponding to the $x - p_x$ phase space in the spatial interval $190< k_0x <290$ in the rear of the target, for k_0L_g =0 (red line), 1(black), and 3 (green).

We can, however, not expect a single hot electron pop-

ulation due to the different acceleration mechanisms at the laser-plasma interface that arise in the simulations. For this reason we adopt the following strategy to determine hot electrons temperatures θ_h from the distributions determined from our simulations. To detect intervals in p_x and equivalently γ in which hot electron populations develop, we integrate the distribution $f(\gamma)$ such that the obtained value of $\int_\gamma^\infty f(\gamma')d\gamma'$ can be associated with the temperature of an equivalent MJ distribution, as developed in the preceding paragraphs. In the high-energy limit, for which Eq. (2) with $dp/d\gamma \to 1$ follows a purely exponential law, the expectation value γ_h defined by the integral over the interval $\gamma' = [\gamma, \infty)$ $\theta_h^{-1} \exp(\gamma/\theta_h) \int_\gamma^\infty \gamma' \exp(-\gamma'/\theta_h) d\gamma' \equiv \gamma + \theta_h$, depending on the lower bound of the integration interval γ, yields a clear relation to the hot electron temperature θ_h. For relativistic *pdf*s governed by a hot electron population, the difference between γ_h and the lower bound of the integration interval γ, namely $\gamma_h - \gamma$ will result in a constant value of θ_h over a given interval in γ.

For the general case $\gamma \geq 1$ (and not only $\gamma^2 \gg 1$) of the electron distribution, the expectation value of γ, with $N_\gamma = 1/(\int_\gamma^\infty f(\gamma')d\gamma')$, can be obtained by integration over an interval in the positive branch of p_x,

$$\gamma_h(\gamma) \equiv N_\gamma \int_\gamma^\infty \gamma' f(\gamma') d\gamma' \ . \tag{4}$$

In simulations the upper bound of the integral is in reality $\gamma_{max} = \sqrt{1 + p_{max}^2} \gg 1$ with vanishing $f(p_{max})$ values.

Consequently, for populations to which a specific temperature θ_h can be associated, the values of $\gamma_h(\gamma) - \gamma$ exhibit plateau-like behavior over an interval in γ. Figure 13 illustrates the formation of two plateau regions, namely in the shaded intervals around $p_x/(m_e c) \simeq 1.7$ and 6, i.e. $\gamma \simeq 2$ and 6, respectively. Figure 14 shows the probability densities $f(p_x)$ corresponding to the curves shown in Fig. 13.

We have consequently determined the hot electron temperatures $\theta_{h,1}$ and $\theta_{h,2}$ for these two electron populations around γ =2 and γ =6, respectively. Their evolution, $\theta_{h,1}$ and $\theta_{h,2}$, as a function of time is shown in Fig. 15(a) and (b), respectively, for the cases with $k_0 L_g$ =0, 1, 3 for the target thickness of $150 k_0^{-1}$. In addition, we show the case with twice the target thickness of L_t =$300 k_0^{-1}$ for $k_0 L_g$ =0 (red dash-dotted line). The time behavior of the temperature $\theta_{h,1}$, seen in Fig. 15 reveals repeated phases of heating and stagnation for the less energetic hot electron population, starting with the arrival of the laser pulse at the laser-plasma interface. Repetitive heating arises when hot electrons circulating through the target return to laser-plasma interface where they are re-accelerated. The period of these acceleration phases is related to the target thickness which is seen both in the phases space images x-p_x and in comparing the hot electron temperature $\theta_{h,1}$ for two cases with the thicknesses L_t =$150 k_0^{-1}$ and $300 k_0^{-1}$, both for $k_0 L_g$ =0 in Fig. 15. The first onset of heating coincides

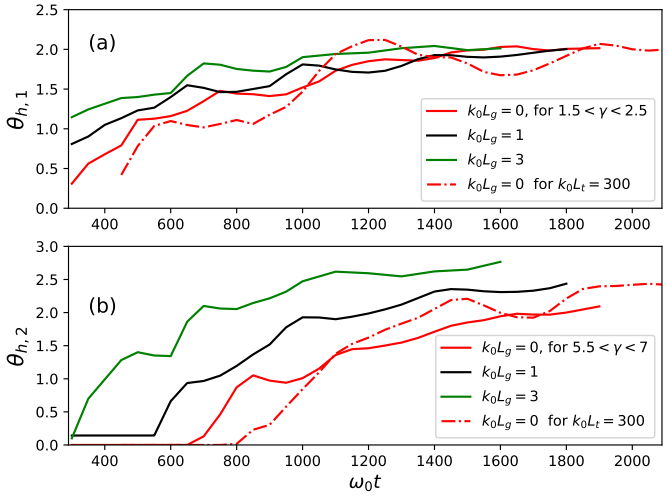

FIG. 15. Hot electron temperatures, $\theta_{h,1}$ (a) and $\theta_{h,2}$ (b), as a function of time, deduced from the expectation values $\gamma_h(\gamma)$, defined in Eq. (4), and γ, for distinct values at which plateau-like behavior is seen in Fig. 13, namely around $p_x/(m_e c)$ =1.7, in the upper plot, and $p_x/(m_e c)$ =6 in the lower subplot, . Cases shown: $k_0 L_g$ =0(red), 1(black), and 3 (green). Solid lines for L_t =$150 k_0^{-1}$, dash-dotted line for $300 k_0^{-1}$.

also with the drop in the reflectivity observed in Fig. 4(a). The heating-stagnation phases are therefore separated typically by $2L_t/c$ being $\sim 300\omega_0^{-1}$ and $\sim 600\omega_0^{-1}$, respectively, which is each time the ballistic circulation time of relativistic electrons. For repeated re-circulation processes this periodicity is smeared out gradually with the increasing dispersion in the length of the trajectory of electrons that are recalled by the ambi-polar field at the rear of the target according to their kinetic energy. The heating of the second, more energetic electron population characterized by $\theta_{h,2}$, here around $p_x/(m_e c)$ =6, is however less linked to re-circulating bunches of electrons. The underlying acceleration mechanism is more related to the presence of energetic electrons in the front part of the target, under the influence of the superposed light fields and therefore to stochastic heating.

IV. EXPANSION OF ION AND ELECTRON PROFILES AT THE REAR LAYER

The values of those hot electron temperatures are useful for models that describe the hydrodynamic expansion of the ion density profile at the rear of the plasma target. The ion front that forms and moves away from the rear face of the plasma, as seen in Figs. 2(b) and 16, corresponds to effective ion acceleration, and is therefore of potential interest for applications (such as proton diagnostics).

Models have been developed for planar expansion, normal to the rear face in x direction. In the context of laser-plasma interaction the assumption of an isothermal equation of state for the electrons is gener-

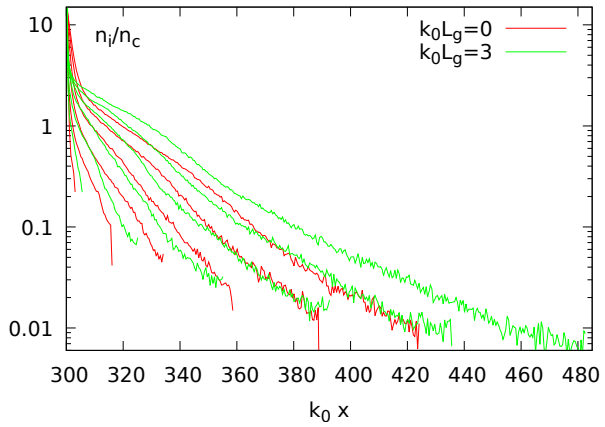

FIG. 16. The ion density profile at the rear of the target for different time instants (from $\omega_0 t$ =300 to 1300 in steps of $\omega_0 \Delta t$ =200), showing a comparison between the two cases with a gradient $k_0 L_g$ =0 (red lines) and 3 (green lines).

ally a good approximation, and for this reason most of the studies are based on an isothermal law for the electron dynamics[2,3,45–47] on the slow, ionic time scale. Those models assume the formation of 'cold (co)' and 'hot (h)' populations characterized by their temperatures T_{co}, T_h and densities n_{co}, n_h, respectively, fulfilling $n_e \equiv n_{co}\exp(e\varphi/k_B T_{co}) + n_h \exp(e\varphi/k_B T_h)$, with k_B denoting the Boltzmann constant. In a similar manner, also the rarefaction for the adiabatic case has been considered[48,49].

For the isothermal case in a semi-finite plasma slab the rarefaction can be considered to follow a similarity law[50] such that the spatial coordinate x and time t can be combined to a single similarity variable $x/(c_s t) \rightarrow \xi + const$ in the set of hydro-dynamic equations for continuity and momentum, with c_s denoting the sound speed of the plasma, $c_s \equiv (Zk_B T/m_i)^{1/2}$, in which Z is the ion charge (here = 1). For the ion density with an exponential law, it follows then for advanced times ($c_s t \gg v_{th,e}/\omega_{pe,0}$)

$$n_i(x,t) = n_{i,0} e^{-[\xi(x,t)+1]} \ , \tag{5}$$

with $\xi \equiv (x - x_r)/(c_s t)$, and x_r denoting the position of the rear face of the plasma at $t = 0$. For what concerns the ion front motion, the plasma temperature T is dominated by the hot electron component $k_B T_h \sim \varepsilon_h$. For the case of constant temperature T_h, the resulting ion velocity is given by $v(x,t)/c_s = (x - x_r)/(c_s t) + 1$, while for a hot electron temperature slowly evolving in time, the sound speed evolves as well, such that one has to replace $c_s t$ by the integral $\int c_s dt$. The balance between the electron pressure and the electrostatic field, $eE_x = -(1/n_e)\partial_x(n_e k_B T_h)$, keeps quasi-neutrality. From Eq. (5) it follows for an isothermal plasma[4]

$$eE_{x,s} = k_B T_h \frac{d\xi}{dx}(x,t) \ . \tag{6}$$

For constant temperature, as assumed in most of the models, this results in $eE_{x,s} = k_B T_h/(c_s t)$ or $E_0/(\omega_{pi} t)$ by involving as ω_{pi} the ion plasma frequency (in the unperturbed plasma) of the hot ('h') electron component, $\omega_{pi} \propto n_h^{1/2}$. Equivalently n_h enters then in the field value $E_0 \equiv (n_h k_B T_h/\epsilon_0)^{1/2}$. For advanced expansion, quasi-neutrality can no longer be maintained in the lower shelf. This occurs when in the plasma profile $c_s t$ equals the local Debye length.[4,50] An expression for the evolution of the electric field at the front for all times, assuming fixed values for T_h and n_h, has been given in Ref. 4, $E_{x,f}(t) = 2E_0 \ / \sqrt{2\exp(1) + \omega_{pi}^2 (t - t_r)^2}$ for $t \geq t_r$ with a reference time t_r, discussed later.

This process has been extensively studied, also with better precision concerning the expression for the ion front. These models assume the (hot) electron temperature as an initial value, but do not consider that the heating is maintained from the front side. Cooling of the hot electron temperature has been considered in models.[51,52] For the case of ongoing heating (or eventual cooling) of the hot electron population, Eq. (6) can be generalized to $eE_{x,s}(t) = k_B T_h(t) \Big/ \int_{t_r}^{t} c_s(t')dt'$, a priori assuming that the temporal change in T_h is not too fast, and that the self-similar character of the solution is preserved and that similarity variable ξ is associated with the path of the ion sound wave $\int c_s dt$.

A. Ion front dynamics

The accelerating electrostatic field that governs the ion front motion can be integrated in time, for which v_f and x_f mark the speed and the position of the ion profile front, beyond which electron cloud has formed.

Both v_f and x_f result by simple integration of the equations of motions

$$\frac{dv_f}{dt} = \frac{Ze}{m_i} E_{x,f} \quad \text{and} \quad \frac{dx_f}{dt} = v_f \ . \tag{7}$$

To examine the range of validity of previous models, it is of interest to consider the case of increasing hot electron temperature in the plasma slab due to the arrival of hot electrons accelerated at the front vacuum (pre-plasma)- dense plasma interface.[4,46,47,53]. With the help of the expression for the isothermal rarefaction, Eq. (5) and replacing $c_s t$ by the integral $\int_{t_r}^{t} c_s(t')dt'$ one has consequently to relate the value of the accelerating electric field to the expansion such that electric field at the ion front, reads in a generalized form with respect to Ref. 4

$$\frac{eE_{x,f}}{m_e \omega_0 c} = \frac{2\theta_h(t)}{\sqrt{2e^1 \frac{n_c}{n_h}\theta_h(t) + (\int_{t_r}^{t} k_0 c_s(t')dt')^2}} \ , \tag{8}$$

wherein n_h denotes the density of the hot electron population and in which the ion sound speed is related to the hot electron temperature via $c_s(t)/c = \sqrt{\theta_h(t) m_e/m_i}$, being a function of time. The first term in the denominator accounts only for the initial value

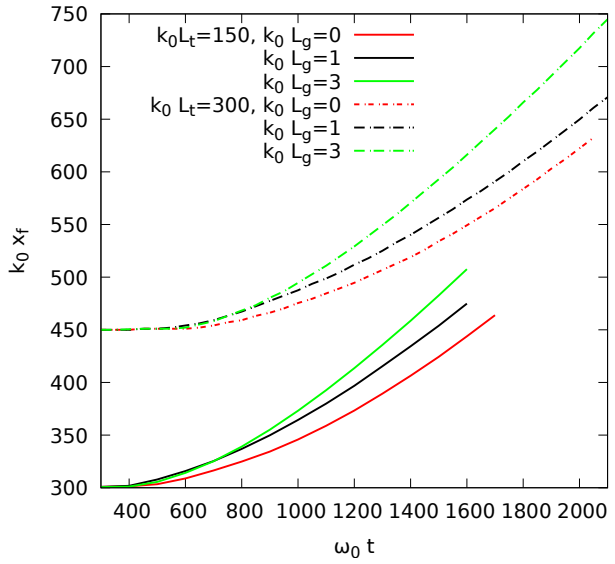

FIG. 17. Time evolution of the ion front position x_f behind the target as a function of time, for both target thicknesses, 150 (solid lines) and $300k_0^{-1}$ (dash-dotted), for the three cases with gradients k_0L_g =0(red), 1(black), and 3(green lines).

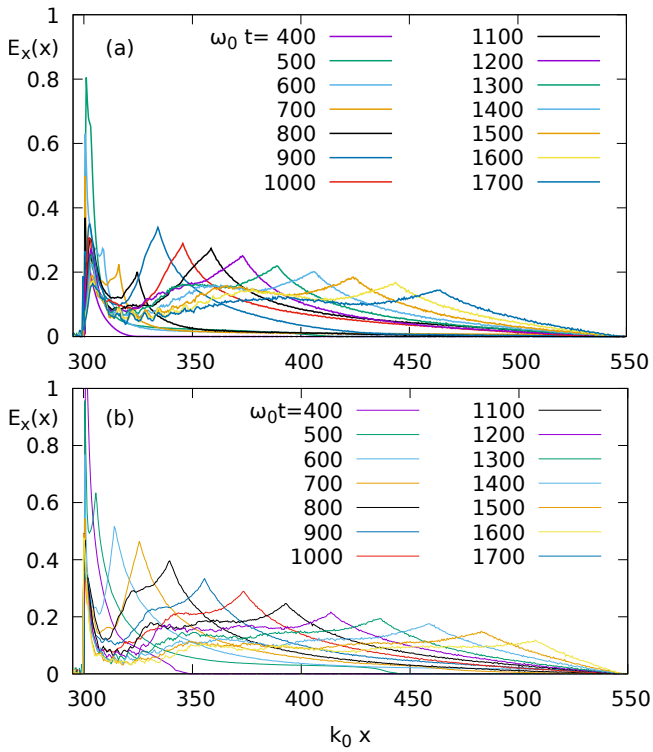

FIG. 18. Spatial profiles, in x, of the electric field $eE_x/(m_e\omega_0 c)$ at the rear side of the target for a sequence of time instants (in steps of $100\omega_0^{-1}$), for the case of target thickness of $150k_0^{-1}$, and for the cases with the gradient k_0L_g =0 (a, upper plot) and k_0L_g =3 (b, lower).

of $E_{x,f}$ while the long time behavior is clearly dominated by the self-similar expansion, $eE_{x,f}/(m_e\omega_0 c) \rightarrow 2\theta_h(t)/\int_{t_r}^{t}\sqrt{\theta_h(t')m_e/m_i}\omega_0 dt'$.

It is therefore essential to understand which hot electron population governs the acceleration process. The dynamics of the ion front described by Eqs. (7) leads to profile expansions shown in Fig. 16 for a series of time instants, and for two cases, a step-like (red lines) interface and an interface with finite gradient (green for $k_0L_g = 3$). The profiles exhibit a sharp ion front that decreases in density with time. The electron profiles, not shown here, follow essentially the part almost up to the front, while their profiles are naturally extended to higher x-values without a sharp front due to the large diffusion of electron energies. From the ion profiles one can conclude that there is a temporal delay between the cases with different gradient length L_g, which is related to the acceleration process of the hot electron populations. This is confirmed in the curves of Fig. 17 and for the time evolution of the ion fronts, deduced from the values in Fig. 16 for all three cases (again red for step-like, black and green for exponential, k_0L_g =1, and 3, respectively). In spite of the difference in the distribution functions, and apart from the time delay due to the different target thickness, the behaviors tend to be very similar. As a matter of fact, the case with the weakest gradient, $k_0L_g = 3$, leads to a more efficient acceleration at the laser-plasma interface, so that the rear expansion is faster. We have determined the spatial profiles of the electric fields E_x for several time instants, shown in Fig. 18 for the cases with k_0L_g =0 and 3, respectively and for a target of the thickness L_t =$150k_0^{-1}$, in which the electric field $E_{x,f}$, at the ion front, is associated with the pronounced peak. Its position moves in time so that we have deduced the time evolution of $E_{x,f}$ for each case from simulations. In Fig. 19 we show the comparison between the cases k_0L_g =0, 1, and 3 for the thickness $150k_0^{-1}$, in Fig. 20 we compare the cases L_t =$150k_0^{-1}$ and $300k_0^{-1}$ for k_0L_g =0 (both).

The temporal evolution of the electric field $E_{x,f}(t)$ seen in Figs.19(a) and 20(a) shows a non-monotonous behavior in time. After the rapid increase when the first hot electrons arrive at the rear of the target, i.e. around $\omega_0 t$ ≃450 and 600 for L_t =$150k_0^{-1}$ and 300, respectively, $E_{x,f}(t)$ decreases first in time, as expected from the model Eq. (8). The transient, quite abrupt increase is a reminiscence of the arrival another hot electron population. The time delay that can be observed is consistent with the evolution of the hot electron temperatures, as seen in Fig. 15.

To account for the two successively arising hot electron populations in our simulations, in the frame of the model equation (8), we have examined several approaches in order to obtain the best agreement with the values $E_{x,f}(t)$ directly deduced from the simulations (Figs.19(a) and 20(a)). We have found the best agreement by applying

the following expression

$$\frac{eE_{x,f}(t)}{m_e\omega_0 c} \equiv \frac{2\theta_{h,1}(t)}{k_0\int_{t_r}^{t} c_{s,1}dt'} + \frac{2\theta_{h,2}(t)}{k_0(\int_{t_r}^{t} c_{s,1}dt' + \int_{t_r}^{t} c_{s,2}dt')}, \quad (9)$$

in which we add the contributions from the hot electron populations, here k =1,2, with their temperatures $\theta_{h,k}(t)$ deduced from the distribution functions, and the corresponding ion sound speed $c_{s,k} = \sqrt{\theta_{h,k}(t)m_e/m_i}$. The results obtained from Eq. (9) are shown in Figs. 19(b) and 20(b). Note that the early time behavior, namely just after the arrival of the first relativistic electron bunches at the rear target interface, is not reconstructed here for which a reliable quantification of the hot electron densities $n_{h,1,2}$ would be necessary. The evolution of $\theta_{h,1}(t)$ and $\theta_{h,2}(t)$ are delayed in time for steep interfaces, k_0L_g =0 and 1, so that $\theta_{h,1}$ governs the motion up to the moment when re-accelerated electrons heat the target bulk, hence $\omega_0 t$ >600 (900)for k_0L_t =150(300). For the case of the weaker gradient, k_0L_g =3 the onset of both hot electron populations is not particularly delayed so that the increment in $E_{x,f}$ is less pronounced. Although the expression Eq. (9) is rather empirical, it yields good agreement for times $\omega_0 t > 450(700)$ for the target thickness k_0L_t =300(600), both what concerns the values at late times and for the transient intervals when the electric field increases again due to the arrival of anther hot spot population.

Note also that the reference time, t_r, being the lower limit of the integrals in the denominators of Eq. (9) have eventually low importance because of the low values of the hot electron temperatures in the early stage, so that the integrals describe naturally the sound wave evolution corresponding to the expansion of the rear profile with evolving hot electron temperatures. The agreement found confirms that, first, the hot electron population '1' with kinetic energies in the interval $0.5 < \gamma - 1 < 1.5$ governs the rear plasma expansion, while, later on, the hotter electron population '2' takes over this role. From the evolution of the ion front, shown in Fig. 21, one can deduce its speed and the corresponding ion energy of the ions in the front. The values, for both cases, reach eventually $v_f/c \sim 0.2 \ldots 0.25$ which corresponds to ion (here proton) energies in the range of 18-30 MeV.

V. DISCUSSION AND CONCLUSIONS

We have examined the acceleration of electrons and ions by laser interaction with a dense plasma target with steep interfaces. Our simulations have been carried out with the particle-in-cell code EMI2D in 2 spatial dimensions and 3 dimensions in momentum space. The cases shown have been computed with the reference parameter $a_0 = 2.8$ corresponding to an incoming laser intensity of 10^{19}W/cm^3 for 1μm wave length. We have limited our study to an initially plane wave field. Our results focus on the motion in the direction of the incoming laser light.

In particular we have studied the sensibility of electron acceleration and heating mechanisms on the gradient of a pre-formed plasma, in focusing on the dynamics normal to direction of incidence. Such finite gradients may originate from pre-formed plasma by a long time-scale foot ('pedestal') of a short laser pulse with insufficient contrast, by a preceding heater beam, or by disintegration of a pre-imprinted surface structure of specially prepared target plasmas, in spite of possible profile steepening.

It is important to mention that the 2D/3D electron motion both across and along the laser propagation is

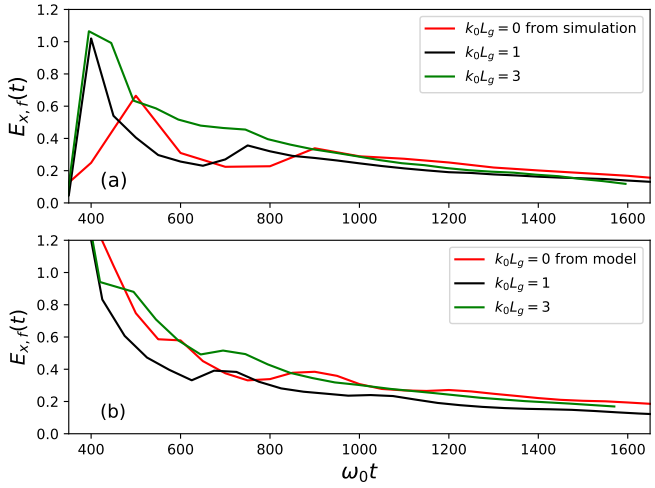

FIG. 19. Time evolution of the electric field $eE_{x,f}/(m_e\omega_0 c)$ at the ion front position behind the target as a function of time, for the case of target thickness of $150k_0^{-1}$. The upper subplot (a) shows a comparison between values deduced from the expansion as in Fig. 18; in (b), below are shown the values deduced in applying Eq. (9) by using θ_h, k-values from Fig. 15. Cases shown: k_0L_g =0 (red line), 1 (black), and 3 (green).

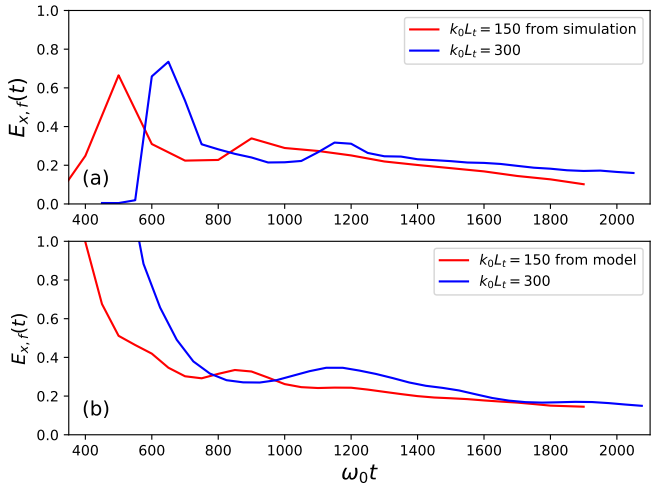

FIG. 20. Time evolution of the electric field $eE_{x,f}/(m_e\omega_0 c)$ at the ion front as a function of time, in subplot (a) deduced from the expansion of the ion front, and in (b) deduced in applying Eq. (9) with the values of Fig. 15. Compared are the cases of target thickness of $150k_0^{-1}$(red) and $300k_0^{-1}$(blue), for k_0L_g =0.

decisive to explain the ongoing acceleration mechanisms. Simulations in only 1D cannot show the essential mechanisms for acceleration because the action of the laser ponderomotive potential blocks the motion in this only direction.

We have considered steep laser-plasma interfaces, with gradient lengths L_g of $k_0 L_g = 0$, 1, and 3, for which the mechanisms in play prove to change the electron dynamics in the incident and reflected laser-light fields in front of the plasma. For those gradients, the motion of electrons, once ejected from the steep gradient interface, is dominated by the standing wave structure of the light fields due to still strong reflection. The motion of relativistic electrons in standing waves leads to stochastic acceleration. Such electrons can then propagate through the dense plasma without that their motion is too much affected (depending on the target thickness). For finite gradients, L_g >0, ponderomotive-type acceleration[21,25] of less energetic bulk electrons arises earlier than stochastic acceleration, and increases the efficiency of the electron heating at earlier times.

The generation of hot electron populations evolves in time and arises via re-circulation of electron through the target and via acceleration of relativistic electron in front of the target. The time of re-circulation, $t_{\rm re}$, can be estimated via the ballistic run time of relativistic electrons, $v_x \simeq \pm c$, namely $t_{\rm re} \sim 2L_t/c$, for the target thickness L_t, to which has to be added the run time through the ambipolar field layer at the rear of the target L_{xf}/c, in which L_{xf} depends on the electron kinetic energy. Electrons can hence be re-accelerated provided that the laser pulse duration t_p is long enough, $t_p > N_{\rm re} t_{\rm re}$, such that electrons returning the $N_{\rm re}$th time still encounter the laser field at the laser-plasma interface.

For simplicity we have carried out the simulations shown here (starting with $T_e \simeq$230eV) without electron-

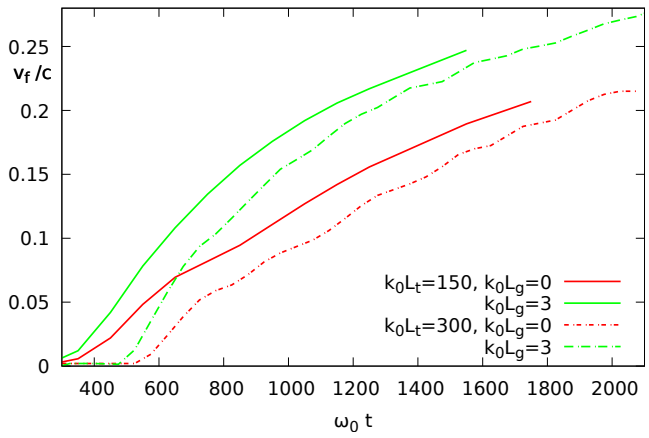

FIG. 21. Time evolution of the ion front velocity v_f behind the target as a function of time, showing a comparison between the cases with gradients $k_0 L_g$ =0(red), and 3(green lines) for the target thickness of L_t =150k_0^{-1} and $k_0 L_g$ =0 (dash-dotted) for L_t =300k_0^{-1} (dash-dotted), .

electron and electron-ion collisions. While the role of collisions remains insignificant for the generation of energetic electrons and the ion expansion governed by hot electron populations, they could contribute indirectly inside the dense plasma via the refluxing of hot electrons and by enhancing the bulk electron temperature.[49,54]

In our simulation we observe hot electron populations, in an early stage around $\gamma \sim 2$ ($p_x \sim 1.7 m_e c$) and then for $\gamma \geq 5$, for which the plateau of the electron distribution widens in time, also depending on the target thickness. The heating process in terms of the hot electrons temperatures evolves in quasi-periodic phases of heating and stagnation, related to $t_{\rm re}$, with loss of synchronization ongoing with time. Collisions between cold thermal and energetic electrons[55], characterized by the temperature T_e and the energy ε, respectively, are very unlikely within the simulation time window due to the fact that the collision frequency ν_{e-e} depends on T_e and ε as $\propto T_e^{-1/2}\varepsilon^{-1}$ instead of the dependence as $\propto T_e^{-3/2}$ for collisions among thermal electrons, because electron distributions develop rapidly into the relativistic regime such that $\varepsilon > 0.5 m_c c^2 > 1000 \times T_e$.

It should be remarked that the physics of the acceleration processes is considerably different in case that the laser pulse duration does not allow, as e.g. in Ref. 8, the formation of a sufficiently extended standing wave structure due to the superposition of the incident and reflected light in front of the plasma. However, even for ultrashort laser pulses, the superposition of the incoming and reflected light field can lead to extremely nonlinear mechanisms, such as the formation of atto-second pulses via high harmonics, see e.g. Ref. 56.

Magnetic fields are induced at the front of the target in the vicinity of the laser-plasma interface and contribute in conjunction with the return current of the bulk due to the hot electron acceleration. Also behind the rear face of the target, in the expanding plasma at lower density than in the bulk, magnetic field structures are excited (here typically with amplitudes $|eB_z/(m_e\omega_0)| \sim 0.5$) that may influence the ion acceleration. However, these fields do not introduce spatial perturbations across the electron and ion density profiles within the simulation time window.

Our simulations show that the ion dynamics at the rear of the target can still be described following the model[4] for the ambi-polar electric field based on the self-similar expansion. This model proves to be robust in spite of the increasing temperatures of hot electron populations that arise during the interaction of electrons with the laser field at the laser-plasma interface.

In experiments with diagnostics that can trace and temporally resolve hot electron populations (e.g. doped targets), the ion front dynamics may hence be post-processed on the basis of this model.

ACKNOWLEDGMENTS

The simulations were granted access to the French HPC resources of IDRIS under the alloca-

tion AD010500573R1 made by GENCI, France. We also thank the CPHT computer team.

[1] L. M. Wickens, J. E. Allen, and P. T. Rumsby, Phys. Rev. Lett. **41**, 243 (1978).
[2] M. A. True, J. R. Albritton, and E. A. Williams, Phys. Fluids **24**, 1885 (1981).
[3] J. E. Crow, P. L. Auer, and J. E. Allen, J. Plasma Physics **14**, 65–76 (1975).
[4] P. Mora, Phys. Rev. Lett. **90**, 185002 (2003).
[5] A. Gurevich, D. Anderson, and H. Wilhelmsson, Phys. Rev. Lett. **42**, 769 (1979).
[6] V. F. Kovalev, V. Y. Bychenkov, and V. T. Tikhonchuk, Journal of Experimental and Theoretical Physics **95**, 226 (2002).
[7] V. F. Kovalev and V. Y. Bychenkov, Phys. Rev. Lett. **90**, 185004 (2003).
[8] V. Y. Bychenkov, V. N. Novikov, D. Batani, V. T. Tikhonchuk, and S. G. Bochkarev, Phys. Plasmas **11**, 3242 (2004).
[9] V. T. Tikhonchuk, A. A. Andreev, S. G. Bochkarev, and V. Y. Bychenkov, Plasma Phys. Control. Fusion **47**, B869 (2005).
[10] D. Khaghani, M. Lobet, B. Borm, L. Burr, F. Gärtner, L. Gremillet, L. Movsesyan, O. Rosmej, M. E. Toimil-Molares, F. Wagner, and P. Neumayer, Scientific Reports **7**, 11366 (2017).
[11] G. Cristoforetti, A. Anzalone, F. Baffigi, G. Bussolino, G. D'Arrigo, L. Fulgentini, A. Giulietti, P. Koester, L. Labate, S. Tudisco, and L. A. Gizzi, Plasma Phys. Contr. Fusion **56**, 095001 (2014).
[12] S. Jiang, L. L. Ji, H. Audesirk, K. M. George, J. Snyder, A. Krygier, P. Poole, C. Willis, R. Daskalova, E. Chowdhury, N. S. Lewis, D. W. Schumacher, A. Pukhov, R. R. Freeman, and K. U. Akli, Phys. Rev. Lett. **116**, 085002 (2016).
[13] G. Cristoforetti, P. Londrillo, P. K. Singh, F. Baffigi, G. D'Arrigo, A. D. Lad, R. G. Milazzo, A. Adak, M. Shaikh, D. Sarkar, G. Chatterjee, J. Jha, M. Krishnamurthy, G. R. Kumar, and L. A. Gizzi, Scientific Reports **7**, 1479 (2017).
[14] L. Torrisi, M. Cutroneo, and A. Torrisi, Contrib. Plasma Phys. **60**, e201900076 (2020).
[15] A. J. Kemp, S. C. Wilks, G. Cochran, S. Kerr, J. Park, G. Grim, and R. Tommasini, Phys. Plasmas **28**, 103102 (2021).
[16] A. Héron, J. C. Adam, and P. Mora, Phys. Plasmas **27**, 013103 (2020).
[17] J. S. DeGroot and J. E. Tull, Phys. Fluids **18**, 672 (1975).
[18] B. Bezzerides, S. J. Gitomer, and D. W. Forslund, Phys. Rev. Lett. **44**, 651 (1980).
[19] F. Brunel, Phys. Rev. Lett. **59**, 52 (1987).
[20] A. J. Kemp, Y. Sentoku, and M. Tabak, Phys. Rev. E **79**, 066406 (2009).
[21] S. C. Wilks, W. L. Kruer, M. Tabak, and A. B. Langdon, Phys. Rev. Lett. **69**, 1383 (1992).
[22] L. Chopineau, A. Leblanc, G. Blaclard, A. Denoeud, M. Thévenet, J.-L. Vay, G. Bonnaud, P. Martin, H. Vincenti, and F. Quéré, Phys. Rev. X **9**, 011050 (2019).
[23] D. Raffestin, L. Lecherbourg, I. Lantuéjoul, B. Vauzour, P.-E. Masson-Laborde, X. Davoine, N. Blanchot, J. Dubois, X. Vaisseau, E. D'Humières, L. Gremillet, A. Duval, C. Reverdin, B. Rosse, G. Boutoux, J. Ducret, C. Rousseaux, and D. Batani, Matter and Radiation at Extremes **6**, 569 (2021).
[24] D. Raffestin, D. Batani, J. Caron, J. Baggio, G. Boutoux, P. Nicolaï, J.-L. Feugeas, V. T. Tikhonchuk, and E. d'Humières, Laser and Particle Beams , 3355928 (2021).
[25] G. J. Williams, A. Link, M. Sherlock, D. A. Alessi, M. Bowers, A. Conder, P. Di Nicola, G. Fiksel, F. Fiuza, M. Hamamoto, M. R. Hermann, S. Herriot, D. Homoelle, W. Hsing, E. d'Humières, D. Kalantar, A. Kemp, S. Kerr, J. Kim, K. N. LaFortune, J. Lawson, R. Lowe-Webb, T. Ma, D. A. Mariscal, D. Martinez, M. J.-E. Manuel, M. Nakai, L. Pelz, M. Prantil, B. Remington, R. Sigurdsson, C. Widmayer, W. Williams, L. Willingale, R. Zacharias, K. Youngblood, and H. Chen, Phys. Rev. E **101**, 031201 (2020).
[26] C. Orban, J. T. Morrison, E. A. Chowdhury, J. A. Nees, K. Frische, S. Feister, and W. M. Roquemore, Physics of Plasmas **22**, 023110 (2015).
[27] A. Héron and J. C. Adam, Phys. Plasmas **22**, 072306 (2015).
[28] C. Thaury, P. Mora, A. Héron, and J. C. Adam, Phys. Rev. E **82**, 016408 (2010).
[29] S. Hüller, A. Porzio, J.-C. Adam, and A. Héron, Phys. Plasmas **26**, 083107 (2019).
[30] Z.-M. Sheng, K. Mima, Y. Sentoku, M. S. Jovanović, T. Taguchi, J. Zhang, and J. Meyer-ter Vehn, Phys. Rev. Lett. **88**, 055004 (2002).
[31] Z.-M. Sheng, K. Mima, J. Zhang, and J. Meyer-ter Vehn, Phys. Rev. E **69**, 016407 (2004).
[32] S. G. Bochkarev, E. d'Humières, V. T. Tikhonchuk, P. Korneev, and V. Y. Bychenkov, Plasma Phys. Contr. Fusion **61**, 025015 (2019).
[33] G. Blaclard, F. Quéré, G. Bonnaud, and H. Vincenti, Phys. Rev. E **107**, 034205 (2023).
[34] D. F. Escande and F. Doveil, J. Stat. Physics **26**, 257 (1981).
[35] G. Schmidt, Comments Plasma Phys. Controlled Fusion **7**, 87 (1982).
[36] J. May, J. Tonge, F. Fiuza, R. A. Fonseca, L. O. Silva, C. Ren, and W. B. Mori, Phys. Rev. E **84**, 025401 (2011).
[37] S. Wilks and W. Kruer, IEEE J. Quant. Electronics **33**, 1954 (1997).
[38] R. Mishra, Y. Sentoku, and A. J. Kemp, Phys. Plasmas **16**, 112704 (2009).
[39] V. M. Ovchinnikov, D. W. Schumacher, M. McMahon, E. A. Chowdhury, C. D. Chen, A. Morace, and R. R. Freeman, Phys. Rev. Lett. **110**, 065007 (2013).
[40] A. Debayle, J. J. Honrubia, E. d'Humières, and V. T. Tikhonchuk, Phys. Rev. E **82**, 036405 (2010).
[41] A. G. Mordovanakis, J. Easter, N. Naumova, K. Popov, P.-E. Masson-Laborde, B. Hou, I. Sokolov, G. Mourou, I. V. Glazyrin, W. Rozmus, V. Bychenkov, J. Nees, and K. Krushelnick, Phys. Rev. Lett. **103**, 235001 (2009).
[42] R. Lichters, J. Meyer-ter-Vehn, and A. Pukhov, Phys. Plasmas **3**, 3425 (1996).
[43] S. V. Bulanov, A. Yogo, T. Z. Esirkepov, J. K. Koga, S. S. Bulanov, K. Kondo, and M. Kando, Phys. Plasmas **22**, 063108 (2015).
[44] F. Jüttner, Annalen der Physik **339**, 856 (1911).
[45] J. S. Pearlman and R. L. Morse, Phys. Rev. Lett. **40**, 1652 (1978).
[46] A. Diaw and P. Mora, Phys. Rev. E **84**, 036402 (2011).
[47] A. Diaw and P. Mora, Phys. Rev. E **86**, 026403 (2012).
[48] T. Kiefer and T. Schlegel, Phys. Plasmas **19**, 102101 (2012).
[49] C. Thaury, P. Mora, J. C. Adam, and A. Héron, Phys. Plasmas **16**, 093104 (2009).
[50] P. Mora and R. Pellat, Phys. Fluids **22**, 2300 (1979).
[51] V. Y. Bychenkov, V. N. Novikov, D. Batani, V. T. Tikhonchuk, and S. G. Bochkarev, Phys. Plasmas **11**, 3242 (2004).
[52] P. Mora, Phys. Rev. E **72**, 056401 (2005).
[53] P. Mora and T. Grismayer, Phys. Rev. Lett. **102**, 145001 (2009).
[54] A. J. Kemp, Y. Sentoku, V. Sotnikov, and S. C. Wilks, Phys. Rev. Lett. **97**, 235001 (2006).
[55] J. D. Huba, *NRL plasma formulary* (Naval Research Lab., Washington, DC, 2013).
[56] N. M. Naumova, J. A. Nees, I. V. Sokolov, B. Hou, and G. A. Mourou, Phys. Rev. Lett. **92**, 063902 (2004).